symmetry

MDPI

Article

Fractional-Order Memory-Enhanced Fixed-Time Anti-Disturbance Tracking Control for Heavy-Duty Cutter-Changing Manipulators Under Payload Jumps and Symmetry Constraints

Shuaikun Zhang [1], Jialin Han [1], Shanshan Huang [2], Xiaoxiong Zhou [2] and Guangming Zhang [2,*]

[1] China Railway Construction Heavy Industry Corporation Limited, Changsha 410131, China; zhangshuaikun@crchi.com (S.Z.); jialinhan@126.com (J.H.)
[2] School of Mechanical Power Engineering, Nanjing Tech University, Nanjing 211816, China; huangss@njtech.edu.cn (S.H.); zhouxx@njtech.edu.cn (X.Z.)
* Correspondence: zgm@njtech.edu.cn

Abstract

Heavy-duty cutter-changing manipulators in shield tunneling operate under abrupt payload attachment and release, extraction impacts, load-dependent friction, model uncertainty, actuator saturation, and measurement noise. These coupled effects can produce large transient tracking errors and excessive actuator demand. This paper develops a fractional-order memory-enhanced fixed-time symmetry-constrained tracking method. Payload-induced inertia variation, gravity mismatch, nonlinear friction, impacts, and unmodeled dynamics are aggregated into a heavy-load lumped disturbance. An acceleration-free momentum residual is combined with a Caputo fractional-order disturbance observer. For each joint, the tracking error is restricted to a zero-centered time-varying symmetric set, and an odd invertible transformation maps the constrained error into an unconstrained coordinate. A fixed-time terminal residual is then constructed in the transformed coordinates. Instead of placing a fractional integral directly in the sliding manifold, the proposed method introduces a nonnegative fractional memory term into the robust reaching gain, which preserves a standard fixed-time Lyapunov certificate while retaining historical residual information. A load-aware gain schedule is generated from the estimated disturbance magnitude. The fractional observer satisfies a componentwise Mittag–Leffler practical-error bound for bounded Caputo derivatives of the filtered input. The ideal sign-based reaching and terminal dynamics admit fixed-time bounds provided that the combined estimation and saturation residual remains below an explicit robustness margin; the smooth finite-memory implementation is evaluated numerically. Numerical studies on a two-link heavy-duty manipulator compare four controllers and examine ablations, fractional-order sensitivity, payload jumps, impacts, saturation and noisy model mismatch. Randomized paired trials quantify the loss of constraint feasibility under uncertain loading and saturation; computational-cost measurements characterize the offline implementation.

Keywords: fractional-order control; fixed-time stability; symmetry constrained control; symmetric error constraints; heavy-duty manipulator; cutter-changing robot; disturbance observer

Check for updates

Academic Editor: Calogero Vetro

Received: 15 September 2026
Revised: 8 October 2026
Accepted: 14 October 2026
Published: 16 October 2026

Copyright: © 2026 by the authors. Licensee MDPI, Basel, Switzerland. This article is an open access article distributed under the terms and conditions of the Creative Commons Attribution (CC BY) license.

1. Introduction

Large-diameter shield tunneling is increasingly dependent on intelligent maintenance equipment that can reduce personnel exposure to confined, high-pressure, and mechani-

cally hazardous excavation environments. Cutter inspection and replacement are particularly demanding because the manipulator must approach the cutterhead, grasp a heavy cutter or tool, overcome extraction resistance, transport the payload through a restricted workspace, and complete insertion and release with high positioning accuracy. Unlike conventional light-duty industrial robots, a cutter-changing manipulator can experience a large payload-to-arm mass ratio, abrupt payload attachment and detachment, strong low-speed friction, short-duration extraction impacts, and strict actuator limits. These features motivate a tracking controller that simultaneously addresses robustness, transient-error regulation, convergence speed, and implementable torque demand.

Trajectory tracking of robotic manipulators has been extensively studied using model-based, adaptive, and sliding-mode methods [1–3]. Sliding-mode control is attractive for uncertain robotic systems because of its matched-disturbance robustness, but conventional designs may exhibit chattering. Finite-time and fixed-time stability provide stronger transient guarantees by making the convergence time finite or independent of the initial condition [4,5]. Recent manipulator studies have further considered fixed-time terminal sliding modes, partially known dynamics, and actuator saturation [6–8]. These advances are relevant to cutter-changing robots. A related fixed-time active fault-tolerant framework for cable-driven parallel robots explicitly enforces admissible cable tensions through quadratic programming [9]; its physical tension allocation problem, however, differs from joint-space symmetric tracking-error constraints under heavy cutter-load transitions. The combined treatment of memory-dependent disturbance estimation, fixed-time joint-space tracking, and time-varying symmetric error bounds remains less developed for cutter-changing duties.

Time-varying symmetric error constraints provide a direct mechanism for regulating transient tracking accuracy. For each joint, a zero-centered admissible set $\mathcal{S}_i(t) = \{e_i : -\rho_i(t) < e_i < \rho_i(t)\}$ is invariant under the sign reversal $e_i \mapsto -e_i$, so positive and negative tracking deviations are treated consistently. The transformed-error construction used in prescribed-performance control provides an effective way to map such a bounded set into an unconstrained coordinate [10]. Related robotic studies have considered assigned-settling-time constraints, terminal sliding modes, event-triggered optimal control, and fault-tolerant tracking [11–14]. Constrained-control developments also include distributed fixed-time control with a fixed-time extended-state observer and feasibility constraints [15], modular formation control with time-varying performance bounds and a finite-time extended-state observer [16], and active-disturbance-rejection tracking of manipulators under a universal symmetry-constraint framework [17]. Disturbance-compensated constrained tracking has also been experimentally investigated for heavy-duty hydraulic manipulators [18]. In the present work, the symmetric error set is incorporated directly into the closed-loop coordinates rather than appended as an auxiliary barrier term, so the constraint $|e_i(t)| < \rho_i(t)$ is retained explicitly in the stability analysis.

Fractional calculus offers a nonlocal mechanism for representing hereditary and memory effects [19–21]. Fractional-order sliding-mode and disturbance-observer techniques have been applied to robotic tracking to improve disturbance rejection and provide additional tuning freedom [22–28]. At the networked-system level, fully distributed dynamic event-triggered observer-based H_∞ consensus has been developed for fractional-order multi-agent systems [29], while recent work has addressed incommensurate fractional-order optimization and output consensus with input saturation [30] and resilient prescribed-time safe optimization under false-data-injection attacks [31]. Fractional-order sliding-mode control under actuator saturation has also been investigated [32]. Nevertheless, a subtle theoretical issue arises when a fractional integral is inserted directly into a sliding manifold and then the vanishing of the manifold is used to claim immediate vanishing of

the non-fractional residual. Because the fractional integral retains the pre-arrival history, such an implication is not generally valid without additional analysis. The present paper therefore uses a different construction: the fixed-time terminal residual remains an ordinary state, whereas the nonnegative fractional memory $I^{\nu}|r|$ enters the robust reaching gain. This preserves the historical-information mechanism without invalidating the fixed-time proof.

Disturbance observation is another key component. A heavy-duty cutter-changing manipulator can be represented by a nominal Euler–Lagrange model plus a lumped disturbance containing payload-dependent inertia error, gravity mismatch, load-dependent friction, external contact forces, and impacts. Disturbance-observer-based tracking has been widely investigated for manipulators, including nonlinear disturbance observation, fixed-time sliding-mode compensation, and adaptive neural disturbance-observer schemes [33–35]. Fixed-time disturbance observation has also been developed for high-order multi-agent systems with actuator faults [36]. Together with the constraint-oriented and fractional-order developments cited above, these results motivate combining disturbance estimation, fixed-time analysis, a symmetric-constraint transformation, and fractional memory in an application-oriented heavy-load framework. In contrast with acceleration-difference observers, the observer used here starts from a measurable generalized-momentum residual, which avoids directly differentiating joint velocity.

Table 1 distinguishes the mathematical roles of closely related designs. The main gap is not simply a lack of fixed-time or fractional-order controllers individually: most available frameworks establish convergence, estimate disturbances, or enforce one particular physical constraint, but do not combine a momentum-based fractional observer, an odd time-varying error transformation, and a history-reinforced reaching gain with an explicit saturation-dependent certificate. The present contribution is this particular coupling, rather than a general claim that fractional memory alone guarantees fixed-time stability.

Table 1. Comparison with related controllers and the present method.

Reference	Main Method	Constraint Type	Distinction Relevant to the Present Study
[22]	Fractional fixed-time SMC for manipulators	Tracking stabilization	No time-varying odd symmetric error transformation with momentum-based FODO
[32]	Fractional sliding mode for space manipulators	Input saturation	Different actuator setting and no nonnegative reaching-memory construction
[8]	Adaptive fixed-time SMC	Input saturation	Does not use a fractional momentum-residual observer
[17]	Disturbance rejection for manipulators	Symmetry constraints	Different observer and fixed-time memory design
[9]	Fixed-time active fault tolerance and QP	Cable tension constraints	Handles physical force allocation rather than symmetric joint tracking errors
Present work	Momentum FODO and mixed-power fixed-time controller	Time-varying symmetric joint-error bounds	Nonnegative fractional reaching memory and explicit conditional saturation-residual analysis

Accordingly, this paper proposes a fractional-order memory-enhanced fixed-time symmetry-constrained controller for heavy-duty cutter-changing manipulators. The main contributions are as follows. First, payload jumps, load-dependent friction, impact loads, parameter mismatch, and actuator saturation residuals are incorporated into a unified heavy-load uncertainty description. Second, an acceleration-free momentum residual and a Caputo fractional-order observer are used for lumped-disturbance reconstruction, while the fixed-time terminal residual is formulated in transformed coordinates associated with a zero-centered symmetric error set. Third, the fractional memory term is introduced into the reaching gain, rather than the manifold itself, so that the memory contribution is nonnegative in the Lyapunov derivative and a conventional fixed-time upper bound is retained. Fourth, load-aware gains are adapted according to the estimated disturbance

magnitude. Finally, the numerical study follows the duty sequence of cutter replacement and includes controller comparisons, ablation studies, fractional-order sensitivity, noise, saturation, parameter mismatch, payload jumps, impact-amplitude sweeps, and a combined extreme-duty case.

The remainder of the paper is organized as follows. Section 2 presents preliminaries and the heavy-load model. Section 3 develops the observer and controller. Section 4 establishes the convergence properties. Section 5 reports the numerical results. Section 6 discusses practical interpretation and limitations, and Section 7 concludes the paper.

2. Preliminaries and Problem Formulation

2.1. Fractional Operators and Fixed-Time Lemma

For a sufficiently regular scalar function $x(t)$, the Caputo derivative of order $0 < \mu < 1$ is defined as

$$ {}^{C}D_t^{\mu} x(t) = \frac{1}{\Gamma(1-\mu)} \int_0^t (t-\tau)^{-\mu} \dot{x}(\tau) d\tau. \tag{1} $$

The Riemann–Liouville fractional integral of order $\nu > 0$ is

$$ I_t^{\nu} x(t) = \frac{1}{\Gamma(\nu)} \int_0^t (t-\tau)^{\nu-1} x(\tau) d\tau. \tag{2} $$

Lemma 1 (Fixed-time comparison lemma)**.** *If a positive definite function V satisfies*

$$ \dot{V} \leq -c_1 V^p - c_2 V^q, \qquad c_1, c_2 > 0, \quad 0 < p < 1 < q, \tag{3} $$

then the origin is fixed-time stable and the settling time satisfies

$$ T \leq \frac{1}{c_1(1-p)} + \frac{1}{c_2(q-1)}, \tag{4} $$

independently of the initial condition [5].

2.2. Heavy-Duty Manipulator Dynamics

Consider an n-DOF cutter-changing manipulator

$$ M(q, m_L)\ddot{q} + C(q, \dot{q}, m_L)\dot{q} + G(q, m_L) + F(\dot{q}, m_L) = \tau_a + d_{\text{ext}}, \tag{5} $$

where $q, \dot{q}, \ddot{q} \in \mathbb{R}^n$ are the joint position, velocity, and acceleration; M is positive definite; $C\dot{q}$ contains Coriolis and centrifugal terms; G is the gravity vector; F contains viscous, Coulomb, Stribeck, and transmission friction; m_L denotes the equivalent payload; d_{ext} contains extraction impacts and external contact forces; and τ_a is the applied actuator torque.

During cutter replacement, the payload may change according to

$$ m_L(t): \quad 0 \longrightarrow m_{\text{tool}} \longrightarrow 0, \tag{6} $$

which represents approach, grasp/extraction, transfer, insertion, and release.

A nominal model is written as

$$ M_0(q)\ddot{q} + C_0(q, \dot{q})\dot{q} + G_0(q) = \tau_a + d_L, \tag{7} $$

where the heavy-load lumped disturbance is

$$ \begin{aligned} d_L =& d_{\text{ext}} - \Delta M(q, m_L)\ddot{q} - \Delta C(q, \dot{q}, m_L)\dot{q} \\ & - \Delta G(q, m_L) - F(\dot{q}, m_L). \end{aligned} \tag{8} $$

Thus,

$$d_L = d_{\text{payload}} + d_{\text{friction}} + d_{\text{impact}} + d_{\text{uncertainty}}. \tag{9}$$

2.3. Actuator Saturation

The actual torque satisfies

$$\tau_a = \text{sat}(\tau_c), \tag{10}$$

with saturation residual

$$\Delta\tau = \tau_a - \tau_c. \tag{11}$$

Hence,

$$M_0\ddot{q} + C_0\dot{q} + G_0 = \tau_c + d_L + \Delta\tau. \tag{12}$$

Assumption 1. *$M_0(q)$ is uniformly positive definite. There exist $\underline{m}, \bar{m} > 0$ such that $\underline{m}I \le M_0(q) \le \bar{m}I$.*

Assumption 2. *On any finite observation horizon $[0, T]$, the lumped disturbance d_L is essentially bounded, $\|d_L(t)\| \le D$, and may have finitely many discontinuities caused by idealized payload switches. Impact forces are finite-amplitude pulses (not Dirac impulses). The momentum filters are consistently initialized, $p_f(0) = p(0)$ and $u_f(0) = 0$.*

Assumption 3. *The desired trajectory q_d, $\dot{q}_d$, and $\ddot{q}_d$ is continuous and bounded. The initial tracking error satisfies the symmetric-constraint feasibility condition $|e_i(0)| < \rho_i(0)$.*

3. Fractional-Order Observer and Fixed-Time Symmetry-Constrained Control

3.1. Acceleration-Free Momentum Residual

Define the nominal generalized momentum

$$p = M_0(q)\dot{q}. \tag{13}$$

Using the standard Euler–Lagrange property that $\dot{M}_0 - 2C_0$ is skew symmetric,

$$\dot{p} = \tau_a + C_0^T\dot{q} - G_0 + d_L. \tag{14}$$

Let

$$u_p = \tau_a + C_0^T\dot{q} - G_0. \tag{15}$$

Then $\dot{p} = u_p + d_L$. Introduce the filters

$$\dot{p}_f = -\lambda_f p_f + \lambda_f p, \qquad \dot{u}_f = -\lambda_f u_f + \lambda_f u_p, \tag{16}$$

and define

$$d_f = \lambda_f(p - p_f) - u_f. \tag{17}$$

Under consistent initialization,

$$d_f(s) = \frac{\lambda_f}{s + \lambda_f} d_L(s), \tag{18}$$

so d_f is an acceleration-free filtered image of the heavy-load disturbance. In the time domain, with $d_f(0) = 0$, the equivalent filter is

$$\dot{d}_f = -\lambda_f d_f + \lambda_f d_L \quad \text{a.e.}, \qquad d_f(t) = \lambda_f \int_0^t e^{-\lambda_f(t-\tau)} d_L(\tau) d\tau. \tag{19}$$

Although d_L may jump at the two payload-switch instants, this convolution is absolutely continuous and does not jump. Since $\|d_f\| \le D$ and $\|\dot{d}_f\| \le 2\lambda_f D$ almost everywhere, its Caputo derivative on the finite interval obeys

$$\left\| {}^{C}D_t^{\mu} d_f(t) \right\| \le \frac{2\lambda_f D T^{1-\mu}}{\Gamma(2-\mu)} =: \bar{\delta}_{\mu}(T), \quad 0 \le t \le T. \tag{20}$$

This gives a sufficient basis for Assumption 2 even at idealized finite payload jumps; it does not cover unbounded impulsive forces. For a uniform-in-time observer bound on an infinite horizon, a separate global bound on $|{}^{C}D_t^{\mu} d_f|$ must be imposed.

3.2. Fractional-Order Disturbance Observer

The disturbance observer is

$${}^{C}D_t^{\mu} \hat{d}_L = -\Omega(\hat{d}_L - d_f), \qquad 0 < \mu < 1, \tag{21}$$

where $\Omega = \mathrm{diag}(\omega_i) > 0$. Define

$$\tilde{d} = d_L - \hat{d}_L. \tag{22}$$

The fractional order μ changes the weighting of the residual history and provides an additional tuning degree of freedom between tracking bandwidth and noise attenuation.

3.3. Symmetric-Constraint Transformation

Let

$$e = q - q_d. \tag{23}$$

For each joint, select

$$\rho_i(t) = (\rho_{i0} - \rho_{i\infty}) e^{-\ell_i t} + \rho_{i\infty}, \tag{24}$$

where $\rho_{i0} > |e_i(0)|$ and $\rho_{i\infty} > 0$. The admissible tracking-error set is

$$\mathcal{S}_i(t) = \{ e_i \in \mathbb{R} : -\rho_i(t) < e_i < \rho_i(t) \}, \qquad \mathcal{S}_i(t) = -\mathcal{S}_i(t), \tag{25}$$

which is symmetric with respect to the origin. Define

$$\zeta_i = \frac{e_i}{\rho_i}, \qquad \xi_i = \mathcal{T}(\zeta_i) = \mathrm{artanh}(\zeta_i) = \frac{1}{2} \ln \frac{1+\zeta_i}{1-\zeta_i}. \tag{26}$$

The mapping is odd, $\mathcal{T}(-\zeta_i) = -\mathcal{T}(\zeta_i)$, and therefore preserves the sign symmetry of the normalized error. Since $\zeta_i = \tanh \xi_i$, finite ξ_i implies

$$-\rho_i(t) < e_i(t) < \rho_i(t), \tag{27}$$

which is equivalent to $|e_i(t)| < \rho_i(t)$.

Let

$$R = \mathrm{diag}\left\{ \frac{1}{\rho_i(1-\zeta_i^2)} \right\}, \qquad \beta = \mathrm{diag}\left\{ \frac{\dot{\rho}_i}{\rho_i} \right\}. \tag{28}$$

Defining

$$h = \dot{q}_d + \beta e, \tag{29}$$

we have

$$\dot{\xi} = R(\dot{q} - h). \tag{30}$$

Differentiation gives

$$\ddot{\xi} = R\ddot{q} + \chi, \tag{31}$$

where

$$\chi = \dot{R}(\dot{q} - h) - R\dot{h}. \tag{32}$$

For implementation, put $\dot{e}_i = \dot{q}_i - \dot{q}_{d,i}$ and $\beta_i = \dot{\rho}_i/\rho_i$. Direct differentiation of $R_i = \rho_i/(\rho_i^2 - e_i^2)$ yields

$$\begin{aligned} \dot{\rho}_i &= -\ell_i(\rho_{i0} - \rho_{i\infty})e^{-\ell_i t}, \qquad \ddot{\rho}_i = \ell_i^2(\rho_{i0} - \rho_{i\infty})e^{-\ell_i t}, \\ \dot{R}_i &= \frac{-\dot{\rho}_i(\rho_i^2 + e_i^2) + 2\rho_i e_i \dot{e}_i}{(\rho_i^2 - e_i^2)^2}, \\ \dot{\beta}_i &= \frac{\ddot{\rho}_i}{\rho_i} - \left(\frac{\dot{\rho}_i}{\rho_i}\right)^2, \end{aligned} \tag{33}$$

$$\dot{h}_i = \ddot{q}_{d,i} + \dot{\beta}_i e_i + \beta_i \dot{e}_i. \tag{34}$$

Consequently, $\chi_i = \dot{R}_i(\dot{q}_i - h_i) - R_i\dot{h}_i$ uses joint positions and velocities, reference derivatives through acceleration, and the known boundary function; no measured $\ddot{q}$ is required. The formulas are valid for $|e_i| < \rho_i$. Numerical clipping used to prevent an invalid logarithm after a constraint violation must not be interpreted as a proof of invariance.

3.4. Fixed-Time Terminal Residual and Fractional Memory

Define

$$\phi(\xi) = A_1 \operatorname{sig}^{\gamma_1}(\xi) + A_2 \operatorname{sig}^{\gamma_2}(\xi), \tag{35}$$

where $A_1, A_2 > 0$ are diagonal,

$$0 < \gamma_1 < 1 < \gamma_2, \tag{36}$$

and $\operatorname{sig}^p(x) = |x|^p \operatorname{sgn}(x)$ componentwise. The terminal residual is

$$r = \dot{\xi} + \phi(\xi). \tag{37}$$

If $r = 0$, then

$$\dot{\xi} = -A_1 \operatorname{sig}^{\gamma_1}(\xi) - A_2 \operatorname{sig}^{\gamma_2}(\xi), \tag{38}$$

which is a standard fixed-time stable system.

The fractional memory is defined as

$$m_\nu(t) = I_t^\nu |r(t)|, \qquad 0 \le \nu < 1, \tag{39}$$

where the absolute value is componentwise. Importantly, $m_\nu(t) \ge 0$. In contrast with placing $I^\nu r$ directly in a sliding manifold, the present design uses m_ν only to reinforce the reaching gain. Thus, historical residual information improves robustness without creating the invalid implication $s = 0 \Rightarrow r = 0$ for a memory-dependent manifold.

3.5. Load-Aware Gains and Control Law

Define a normalized estimated-load index

$$\eta_L(t) = \operatorname{sat}\left(\frac{\|\hat{d}_L(t)\|}{d_{\text{ref}}}\right) \in [0, 1]. \tag{40}$$

The reaching gains are

$$K_j(t) = K_{j0} + K_{jL}\eta_L(t), \qquad j \in \{1, 2, r\}. \tag{41}$$

Define

$$\begin{aligned} v_{\xi} = &-\dot{\phi}(\xi) - K_1(t)\,\mathrm{sig}^{a}(r) - K_2(t)\,\mathrm{sig}^{b}(r) \\ &- \left[K_r(t) + K_f m_v(t)\right]\mathrm{sgn}(r), \end{aligned} \tag{42}$$

where $0 < a < 1 < b$ and $K_f > 0$ is diagonal. The command torque is

$$\tau_c = C_0(q,\dot{q})\dot{q} + G_0(q) + M_0(q)R^{-1}\left(v_{\xi} - \chi\right) - \hat{d}_L. \tag{43}$$

Substituting (43) into (12) and using (31) gives

$$\ddot{\xi} = v_{\xi} + w, \qquad w = RM_0^{-1}(\tilde{d} + \Delta\tau). \tag{44}$$

Therefore,

$$\begin{aligned} \dot{r} = &-K_1\,\mathrm{sig}^{a}(r) - K_2\,\mathrm{sig}^{b}(r) \\ &- \left(K_r + K_f m_v\right)\mathrm{sgn}(r) + w. \end{aligned} \tag{45}$$

For numerical implementation, $\mathrm{sgn}(r)$ is replaced by $\tanh(r/\varepsilon_r)$, and the fractional operators are implemented using a finite-memory Grünwald–Letnikov approximation. The exact fixed-time result below applies to the ideal sign law, not automatically to this regularized discrete-time realization.

4. Stability Analysis

Theorem 1 (Fractional-observer practical convergence)**.** *Under Assumptions 1 and 2, let* $e_o = \hat{d}_L - d_f$ *and* $\delta_{\mu,i}(t) = {}^{C}D_t^{\mu} d_{f,i}(t)$*, with* $|\delta_{\mu,i}(t)| \le \bar{\delta}_{\mu,i}$ *on the observation interval. For the diagonal gain* $\Omega = \mathrm{diag}(\omega_i) > 0$*,*

$$|e_{o,i}(t)| \le E_{\mu}(-\omega_i t^{\mu})|e_{o,i}(0)| + \frac{\bar{\delta}_{\mu,i}}{\omega_i}\left[1 - E_{\mu}(-\omega_i t^{\mu})\right]. \tag{46}$$

Here E_{μ} *is the one-parameter Mittag–Leffler function. The actual lumped-disturbance error therefore satisfies*

$$|\tilde{d}_i(t)| \le |d_{L,i}(t) - d_{f,i}(t)| + |e_{o,i}(t)|. \tag{47}$$

Proof. Linearity of the Caputo derivative gives

$${}^{C}D_t^{\mu} e_{o,i} = -\omega_i e_{o,i} - \delta_{\mu,i}(t). \tag{48}$$

The variation-of-constants formula is

$$e_{o,i}(t) = e_{o,i}(0)E_{\mu}(-\omega_i t^{\mu}) \tag{49}$$

$$- \int_0^t (t-\tau)^{\mu-1} E_{\mu,\mu}[-\omega_i (t-\tau)^{\mu}]\delta_{\mu,i}(\tau)d\tau. \tag{50}$$

For $0 < \mu < 1$ and $\omega_i > 0$, the Mittag–Leffler resolvent kernel $(t-\tau)^{\mu-1}E_{\mu,\mu}[-\omega_i(t-\tau)^{\mu}]$ is nonnegative, and its integral is $[1 - E_{\mu}(-\omega_i t^{\mu})]/\omega_i$. Applying the upper bound on $|\delta_{\mu,i}|$ to the convolution yields (46) without an unspecified multiplicative constant. Equation (47) follows from $\tilde{d} = (d_L - d_f) - (\hat{d}_L - d_f)$. When d_L has a finite jump, d_f stays continuous by (19) and its Caputo derivative remains bounded over a finite time interval by (20). Thus no value of ${}^{C}D_t^{\mu} d_f$ must be assigned at an idealized Dirac impulse. □

Remark 1. *The observer is intentionally characterized by Mittag–Leffler practical convergence instead of exact finite-time convergence. This avoids attributing a strict finite-time sticking property to an ordinary Caputo state whose derivative retains the history prior to the convergence instant.*

Explicit Disturbance and Saturation Residual Budget

The bound on w must be established rather than inferred from actuator limits alone. For componentwise clipping at $\tau_{\max,j} > 0$,

$$|\Delta\tau_j| = \max\{0, |\tau_{c,j}| - \tau_{\max,j}\}. \tag{51}$$

If $|\tau_{c,j}| \le U_j$ on a specified operating region, then $|\Delta\tau_j| \le \bar{\Delta}_j = (U_j - \tau_{\max,j})_+$. Suppose that this region is such that $\rho_i(t) \ge \rho_{i\infty}$, $|\zeta_i(t)| \le z_* < 1$, and the estimation-error bound in (47) is $|\tilde{d}_j| \le D_j^*$. Directly from (44),

$$\begin{aligned} |w_i(t)| &\le |R_i| \sum_{j=1}^{n} |(M_0^{-1})_{ij}| \left(D_j^* + \bar{\Delta}_j\right) \\ &\le \frac{\sqrt{n}}{\underline{m}\rho_{i\infty}(1 - z_*^2)} \left\|D^* + \bar{\Delta}\right\|_\infty =: W_i^*. \end{aligned} \tag{52}$$

Here $\|M_0^{-1}\|_\infty \le \sqrt{n}/\underline{m}$ follows from uniform positive definiteness. A conservative sufficient condition is $k_{r,i}^{\min} > W_i^*$ for each i. Stronger and simpler torque feasibility, $U_j \le \tau_{\max,j}$, gives $\bar{\Delta}_j = 0$. These are *conditional* operating-region certificates; bounded actuator torque alone cannot ensure small $\Delta\tau$ because the unsaturated command τ_c may grow. In particular, R_i diverges as $|\zeta_i| \uparrow 1$, so a global saturation-independent bound cannot be claimed without a separate robust invariant-region or input-feasibility argument. Saturated simulations test whether the trajectory remains within the bounds in the stated cases but are not a mathematical proof of this sufficient condition.

Theorem 2 (Fixed-time symmetry-constrained tracking)**.** *Consider the closed-loop system under* (43) *with the ideal discontinuous sign law. Suppose Assumptions 1–3 hold and that a forward operating region admits the explicit bound* $|w_i(t)| \le W_i^*$ *from* (52) *along its closed-loop trajectories. If*

$$k_{r,i}^{\min} > W_i^*, \tag{53}$$

$0 < a < 1 < b$, *and* $0 < \gamma_1 < 1 < \gamma_2$, *then* r *reaches zero within an initial-condition-independent fixed time for trajectories satisfying that certificate. Thereafter,* ξ *converges to zero in a fixed time independent of its initial value. Moreover, the original tracking error remains in the symmetric set* $\mathcal{S}_i(t)$, *equivalently* $|e_i(t)| < \rho_i(t)$, *for all* $t \ge 0$. *For the smooth implementation* $\mathrm{sgn}(r) \mapsto \tanh(r/\varepsilon_r)$, *a fixed-time entrance bound to a residual neighborhood holds under the same disturbance budget; exact finite-time convergence is not asserted.*

Proof. For the ith component, choose $V_i = |r_i|$. From (45), the nonnegative memory term $m_{v,i} = I^v|r_i|$ gives

$$\begin{aligned} \dot{V}_i &\le -k_{1i}|r_i|^a - k_{2i}|r_i|^b - \left(k_{ri} + k_{fi}m_{v,i} - |w_i|\right) \\ &\le -k_{1i}^{\min} V_i^a - k_{2i}^{\min} V_i^b, \end{aligned} \tag{54}$$

where (53) and $m_{v,i} \ge 0$ have been used. Lemma 1 therefore yields

$$T_{r,i} \le \frac{1}{k_{1i}^{\min}(1-a)} + \frac{1}{k_{2i}^{\min}(b-1)}. \tag{55}$$

Hence r reaches the origin in a fixed time $T_r \leq \max_i T_{r,i}$. On $r = 0$, (37) becomes the fixed-time system (38), and another application of Lemma 1 gives

$$T_{\xi,i} \leq \frac{1}{a_{1i}(1-\gamma_1)} + \frac{1}{a_{2i}(\gamma_2 - 1)}. \tag{56}$$

Thus $T \leq T_r + \max_i T_{\xi,i}$ is independent of the initial state on the region in which (52) holds. Before T_r, the right-hand side of $\dot{\xi} = r - \phi(\xi)$ is finite for finite r, and the stabilizing mixed-power term prevents finite escape; therefore $\xi(t)$ remains finite. Since $e_i = \rho_i \tanh \xi_i$, finiteness of ξ_i implies $|e_i(t)| < \rho_i(t)$ for all t. For the regularized reaching term, select any $\delta_i > 0$ such that $k_{r,i}^{\min} \tanh(\delta_i/\varepsilon_r) > W_i^*$. Whenever $|r_i| \geq \delta_i$, the comparison inequality (54) still holds, implying a fixed-time upper bound for entrance into $|r_i| \leq \delta_i$. Within this layer, $\dot{\xi}_i = -\phi_i(\xi_i) + r_i$ is input-to-state practically stable; therefore, only practical tracking convergence follows for the regularized implementation. The finite-memory discrete controller is further subject to discretization and measurement errors. □

Remark 2. *The importance of Theorem 2 is a precise separation between a theoretically certifiable fixed-time mechanism and a fractional nonnegative gain modifier. Unlike an unconstrained terminal controller, the terminal residual evolves in the odd transformed coordinates associated with the symmetric admissible error set. The result is conditional on a verifiable input/disturbance budget and does not certify arbitrary external shocks or excessive saturation. The fractional memory does not carry the fixed-time proof by itself. Its role is to reinforce the robust gain according to the accumulated residual history. The fixed-time certificate is supplied by the integer-order mixed-power terms in* (45)*. This separation is deliberate and avoids a common ambiguity in memory-dependent sliding manifolds.*

5. Numerical Validation

5.1. Simulation Setup and Reproducibility

A two-link heavy-duty manipulator is used to evaluate the closed-loop behavior under severe loading conditions. The model is parameterized at a substantially higher mass and torque level than a typical laboratory arm so that payload change, impact loading, friction, and saturation effects are visible. The principal simulation and controller parameters are summarized in Table 2. The numerical values in the tables and the accompanying figures correspond to the reported simulation cases; the parameter settings and performance metrics are defined below.

Table 2. Main simulation parameters.

Symbol	Value	Meaning
m_1, m_2	45, 30 kg	nominal link masses
l_1, l_2	0.75, 0.60 m	link lengths
m_L	$0 \to 35 \to 0$ kg	payload profile
μ	0.72	fractional observer order
ν	0.38	fractional memory order
γ_1, γ_2	0.72, 1.30	terminal exponents
a, b	0.68, 1.28	reaching exponents
λ_f	30	momentum-filter bandwidth
Ω	$[18, 18]^\top$	observer gains
K_f	$[5, 5]^\top$	fractional memory gains
ρ_0	$[0.40, 0.35]^\top$	initial symmetric error bounds
ρ_∞	$[0.055, 0.050]^\top$	steady symmetric error bounds
$\tau_{\max}$	$[1050, 700]^\top$ Nm	extreme-duty torque limits
h	0.002 s	simulation step
T	12 s	simulation horizon

For N recorded samples with sampling interval h, the reported joint root-mean-square error, integral absolute error, normalized constraint ratio, and empirical violation count are computed as

$$\mathrm{RMSE}_i = \sqrt{\frac{1}{N}\sum_{k=1}^{N} e_i(t_k)^2}, \qquad \mathrm{IAE} = h\sum_{k=1}^{N}\sum_{i=1}^{n}|e_i(t_k)|, \tag{57}$$

$$\mathcal{R}_{\max} = \max_{i,k}\frac{|e_i(t_k)|}{\rho_i(t_k)}, \qquad N_{\mathrm{viol}} = \sum_{k=1}^{N}\mathbf{1}\{\exists i : |e_i(t_k)| \geq \rho_i(t_k)\}. \tag{58}$$

The reported recovery time is the first instant following the $t = 4.8$ s extraction impact for which $\|e\|_2 < 0.05$ rad persists for at least 0.10 s. A zero violation count is evidence about the sampled trajectory, not a continuous-time proof between sample instants.

The desired trajectory is

$$q_{d,1}(t) = 0.32\sin(0.45t) + 0.12\sin(0.9t), \tag{59}$$

$$q_{d,2}(t) = -0.28\sin(0.45t + 0.35) + 0.10\sin(0.75t). \tag{60}$$

The payload profile is

$$m_L(t) = \begin{cases} 0, & t < 2.5\ \mathrm{s}, \\ 35\ \mathrm{kg}, & 2.5 \leq t < 8.5\ \mathrm{s}, \\ 0, & t \geq 8.5\ \mathrm{s}. \end{cases} \tag{61}$$

Two Gaussian impact pulses model extraction and insertion shocks:

$$d_{\mathrm{impact}} = D_{\mathrm{imp},1}e^{-((t-4.8)/0.06)^2} + D_{\mathrm{imp},2}e^{-((t-8.35)/0.08)^2}, \tag{62}$$

where $D_{\mathrm{imp},1}$ and $D_{\mathrm{imp},2}$ are joint-space impact-amplitude vectors. The load-dependent Stribeck friction is

$$F_i = \left[F_{c,i} + (F_{s,i} - F_{c,i})e^{-(\dot{q}_i/v_{s,i})^2}\right]\tanh\left(\frac{\dot{q}_i}{\epsilon_v}\right) + B_i\dot{q}_i, \tag{63}$$

where F_c and B increase with m_L. In the simulation, $F_c = [16, 12]^\top(1 + 0.012m_L)$ N m, $F_s = 1.35F_c$, $B = [18, 14]^\top(1 + 0.008m_L)$ N m s/rad, $v_s = [0.08, 0.07]^\top$ rad/s, and $\epsilon_v = 0.01$ rad/s; the model-mismatch scenario multiplies friction by 1.12. The impact vectors are $D_{\mathrm{imp},1} = 0.75[180, -120]^\top$ N m and $D_{\mathrm{imp},2} = 0.75[-140, 90]^\top$ N m in the main comparison. The initial state is $q(0) = [0.16, -0.12]^\top$ rad, $\dot{q}(0) = 0$, and the observer state is initialized at zero.

The extreme-duty scenario simultaneously applies a 35 kg payload, both impact pulses, 12% and 8% base-link mass mismatch, a 3% gravity-model mismatch, a 12% friction increase, encoder/velocity noise, and torque saturation at $[1050, 700]^\top$ N m. Table 3 lists the comparison-controller settings to support reproducibility and parameter-level comparison.

Table 3. Controller settings used in the comparison.

Controller	Main Settings	Observer	Symmetric Constraint	Load-Aware
CTC	$K_p = 22I$, $K_d = 10I$	No	No	No
SMC	$\lambda = 5.5$, $k_s = 18$, boundary-layer width 0.04	No	No	No

Table 3. *Cont.*

Controller	Main Settings	Observer	Symmetric Constraint	Load-Aware
NFTSMC	$A_1 = \mathrm{diag}(4.0, 4.2)$, $A_2 = \mathrm{diag}(1.25, 1.30)$, $\gamma_1 = 0.72$, $\gamma_2 = 1.30$, $a = 0.68$, $b = 1.28$, $k_1 = 9$, $k_2 = 2.5$, $k_r = 18$	No	No	No
Proposed	$A_1 = \mathrm{diag}(4.0, 4.2)$, $A_2 = \mathrm{diag}(1.25, 1.30)$, $K_{10} = 9I$, $K_{20} = 2.5I$, $K_{r0} = 16I$, $K_f = 5I$, $\Omega = 18I$	FODO	Yes	Yes

5.2. Tracking Under Symmetric Error Constraints

Figure 1 shows the proposed-controller trajectories under the combined extreme-duty condition. The payload is attached at 2.5 s, the principal extraction impact occurs at 4.8 s, and the payload is released near 8.5 s. The tracking curves remain close to their references despite the sudden load and impact changes.

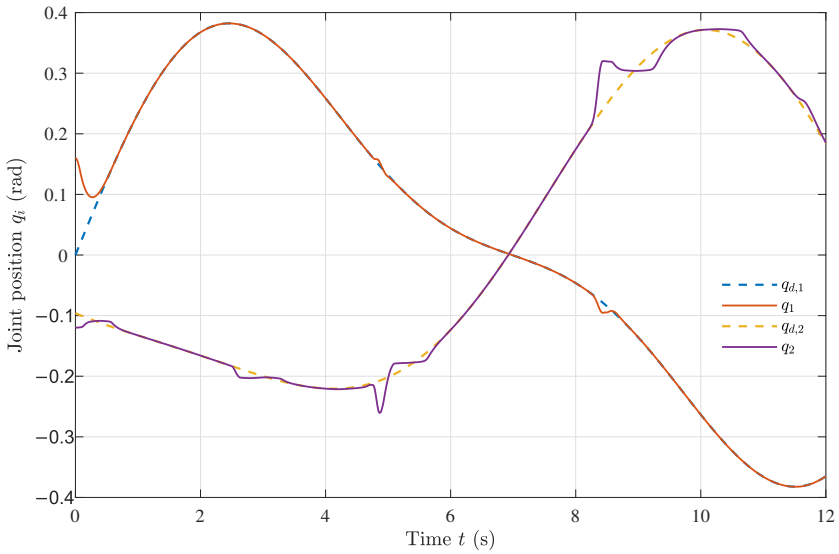


Figure 1. Joint tracking under the combined extreme-duty cycle.

Figure 2 shows the tracking errors together with the positive and negative symmetric bounds. The maximum normalized ratio $\max |e_i|/\rho_i$ remains below unity in the full proposed case, confirming that the trajectories remain inside $\mathcal{S}_i(t)$ throughout the simulated duty cycle.

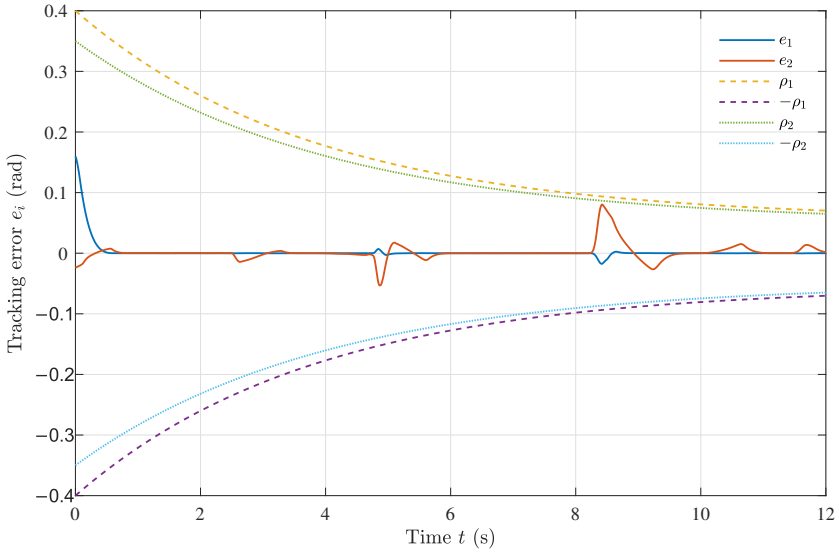


Figure 2. Tracking errors and zero-centered symmetric time-varying bounds.

5.3. Disturbance Observation and Actuator Demand

Figure 3 compares the nominal-model lumped disturbance and the fractional-order estimate. The observer follows the payload/friction component and reacts to the short impact pulses with finite lag, as expected for a memory filter. The noisy estimates reflect finite-bandwidth reconstruction of load-dependent effects; since the residual uses measured momentum, no explicit velocity differentiation is performed. The distinction between estimating d_L and its filtered image d_f is important during short impact pulses (Figure 3).

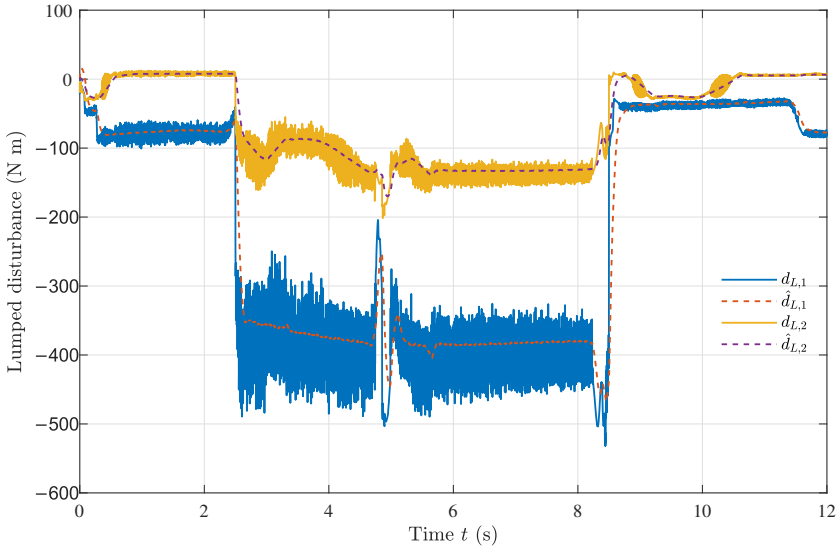


Figure 3. Lumped disturbance and fractional-order disturbance estimate.

Figure 4 gives the applied actuator torques and the imposed limits. In the combined extreme-duty case, the first actuator reaches its limit for a short interval, so the saturation model is active rather than merely present symbolically.

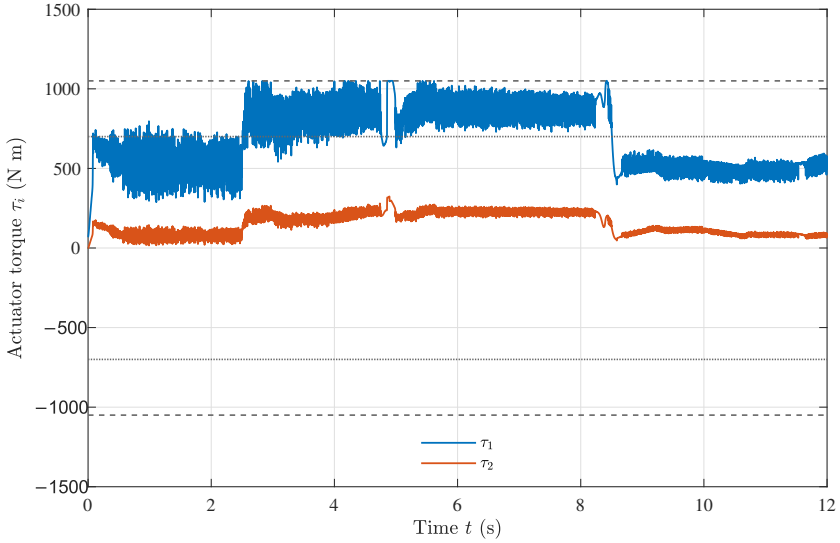


Figure 4. Applied actuator torques and saturation limits.

5.4. Controller Comparison

CTC, conventional SMC, NFTSMC, and the proposed method are compared under the same extreme-duty scenario. Table 4 reports RMSE, integral absolute error (IAE), saturation ratio, recovery time after the first extraction impact, and the maximum normalized constraint ratio. Under the combined extreme-duty condition, the proposed controller

gives joint RMSE values of 0.0147 and 0.0135 rad, compared with 0.0157 and 0.0840 rad for NFTSMC. Its joint-2 RMSE and IAE decrease by 83.9% and 82.0%, respectively, relative to NFTSMC. The recovery time to $\|e\|_2 < 0.05$ rad after the first impact is 0.096 s. These are numerical outcomes of the specified scenario, not universal error guarantees. Figure 5 helps separate the improvement in the more vulnerable second joint from the comparatively small first-joint difference. The 1.02% saturation ratio for the proposed controller also confirms that its results are not obtained by removing the actuator limits.

Table 4. Controller performance under the combined extreme-duty scenario.

Controller	$\mathbf{RMSE_1}$	$\mathbf{RMSE_2}$	IAE	Sat. (%)	T_{rec} (s)	Max $\|e\|/\rho$
CTC	0.2554	0.2555	4.921	0.00	–	6.613
SMC	0.0206	0.1227	0.917	5.00	0.522	4.660
NFTSMC	0.0157	0.0840	0.562	5.55	0.358	2.806
Proposed	0.0147	0.0135	0.101	1.02	0.096	0.929

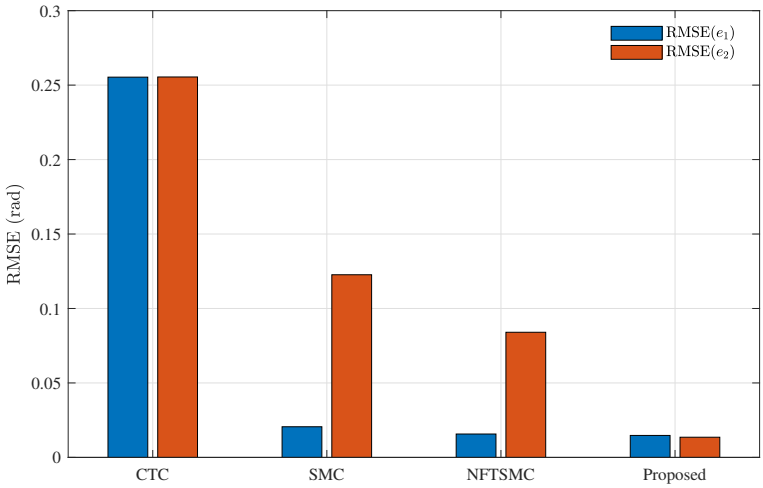


Figure 5. RMSE comparison under the combined extreme-duty scenario.

Figure 6 enlarges the time interval around the principal extraction impact. The recovery time decreases from 0.358 s for NFTSMC to 0.096 s for the proposed method, a 73.2% reduction in this run. Figure 6 also shows that the baseline residual persists for longer after the 4.8 s impact, a behavior relevant to subsequent cutter transfer.

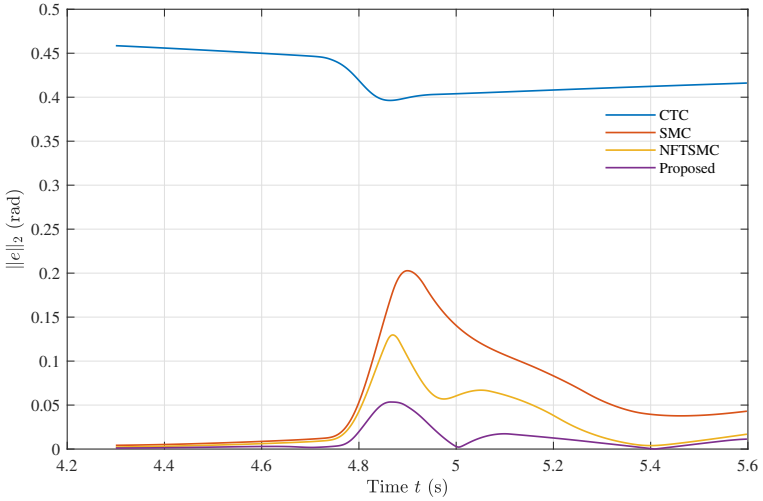


Figure 6. Tracking-error norm around the principal extraction impact.

5.5. Ablation Study

To isolate the contribution of each element, the proposed controller is compared with four ablated variants: removal of the fractional-order disturbance compensation (NoFODO), removal of the fractional memory gain (NoMemory), fixed rather than load-aware reaching gains (FixedGain), and removal of the symmetric-constraint transformation (NoSC). The results are summarized in Table 5 and Figure 7. Removing the disturbance observer produces the largest degradation because the nominal model is intentionally subjected to a large payload mismatch. Compared with the complete design, removing the memory term changes the IAE from 0.101 to 0.115 rad s (an increase of 13.9% relative to the complete method), a smaller effect than removing observer compensation. Freezing the gains increases the recovery error, while removing the symmetric-constraint transformation leads to pronounced bound violation under saturation and impact loads.

Table 5. Ablation study under the extreme-duty scenario.

Variant	$\mathbf{RMSE_1}$	$\mathbf{RMSE_2}$	IAE	Sat. (%)	Max $\|e\|/\rho$
Proposed	0.0147	0.0135	0.101	1.02	0.929
NoFODO	0.4304	0.2427	6.361	1.48	8.698
NoMemory	0.0149	0.0148	0.115	1.03	0.956
FixedGain	0.0149	0.0169	0.124	0.47	1.021
NoSC	0.0668	0.3322	2.273	21.93	10.275

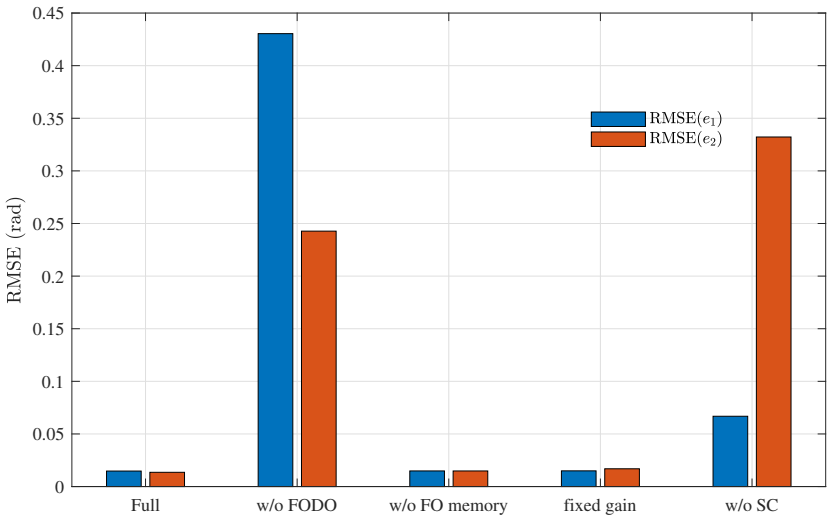


Figure 7. Ablation comparison under the combined extreme-duty scenario.

5.6. Fractional-Order Sensitivity

The observer order and memory order are varied over

$$\mu \in \{0.55, 0.65, 0.72, 0.80, 0.90\}, \qquad \nu \in \{0, 0.20, 0.38, 0.55, 0.70\}. \tag{64}$$

Here $\nu = 0$ represents the order-zero, memoryless limiting case $I^0|r| = |r|$; the separate NoMemory ablation sets $K_f = 0$. Figure 8 shows the combined RMSE for the resulting 25 combinations. The numerical grid is tabulated in Table 6. The sweep characterizes the sensitivity of the closed-loop response to the two fractional orders and quantifies the associated robustness–memory tradeoff. In this benchmark, lower μ tends to reduce combined RMSE, whereas large μ and large ν can increase the peak normalized constraint ratio because the observer/memory layers react more slowly to the short impact pulse.

Table 6. Combined tracking RMSE (rad) for the observer-order and memory-order grid.

$\mu \backslash \nu$	**0.00**	**0.20**	**0.38**	**0.55**	**0.70**
0.55	0.0191	0.0196	0.0206	0.0210	0.0212
0.65	0.0200	0.0205	0.0213	0.0218	0.0220
0.72	0.0209	0.0216	0.0220	0.0223	0.0221
0.80	0.0215	0.0229	0.0237	0.0239	0.0240
0.90	0.0228	0.0244	0.0250	0.0252	0.0254

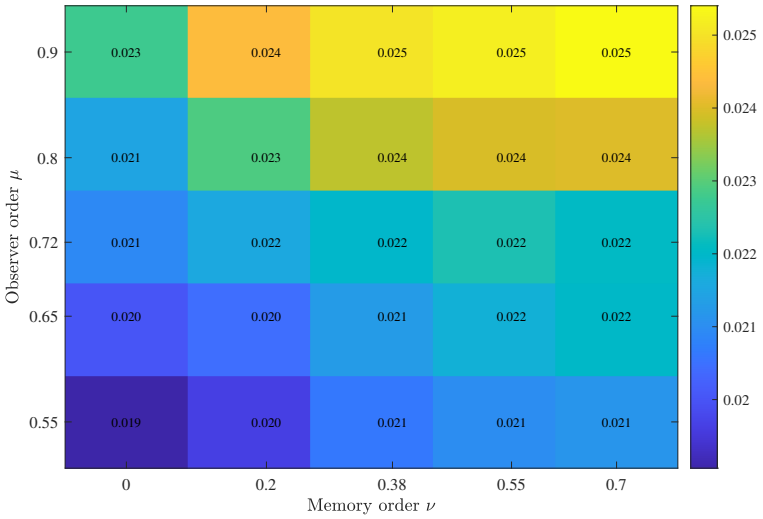


Figure 8. Sensitivity of combined RMSE to the fractional observer order μ and memory order ν.

5.7. Robustness Under Individual and Combined Extreme Conditions

Seven scenarios are examined: nominal motion, payload change only, payload plus impacts, model mismatch, measurement noise, a saturation-focused case, and the complete extreme-duty condition. Table 7 and Figure 9 show that the proposed controller maintains low RMSE across the individual perturbations. The combined case is more demanding because it includes simultaneous model mismatch, noise, impacts, and active torque limitation; for example, its joint-2 RMSE is 0.0135 rad compared with 0.0033 rad in nominal operation (Table 7). Nevertheless, the maximum normalized constraint ratio remains below unity in the representative run.

Table 7. Robustness of the proposed controller under progressively severe scenarios.

Scenario	**RMSE$_1$**	**RMSE$_2$**	**IAE**	**Sat. (%)**	**Max $\lvert e \rvert / \rho$**
nominal	0.0147	0.0033	0.040	0.00	0.400
payload	0.0147	0.0047	0.051	0.00	0.400
impact	0.0148	0.0132	0.092	0.00	0.933
model	0.0146	0.0050	0.053	0.00	0.400
noise	0.0147	0.0047	0.052	0.00	0.400
saturation	0.0148	0.0132	0.092	0.00	0.933
extreme	0.0147	0.0135	0.101	1.02	0.929

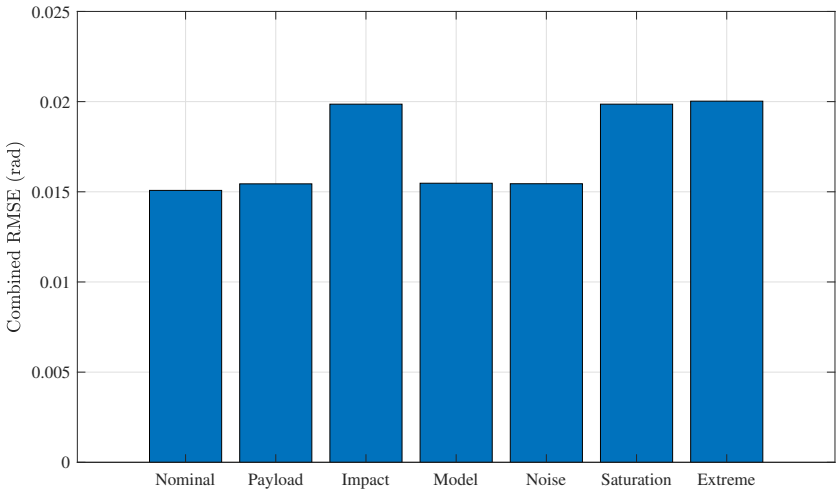


Figure 9. Combined RMSE of the proposed controller under progressively severe scenarios.

5.8. Impact-Amplitude Sweep

Finally, the impact amplitude is scaled from 0.5 to 1.5 times the nominal value. Figure 10 plots the recovery time, while Table 8 lists the underlying metrics. For moderate impact levels the controller rapidly restores the tracking trajectory; when the impact scale exceeds the nominal design case, recovery time increases because the actuator limit becomes dominant. The sweep distinguishes closed-loop robustness from the physical limitation imposed by actuator saturation under increasingly severe shocks.

Table 8. Impact-amplitude sensitivity of the proposed controller.

Impact Scale	Combined RMSE (rad)	Recovery Time (s)
0.50	0.0170	0.000
0.75	0.0200	0.096
1.00	0.0285	0.140
1.25	0.0476	1.302
1.50	0.0958	2.390

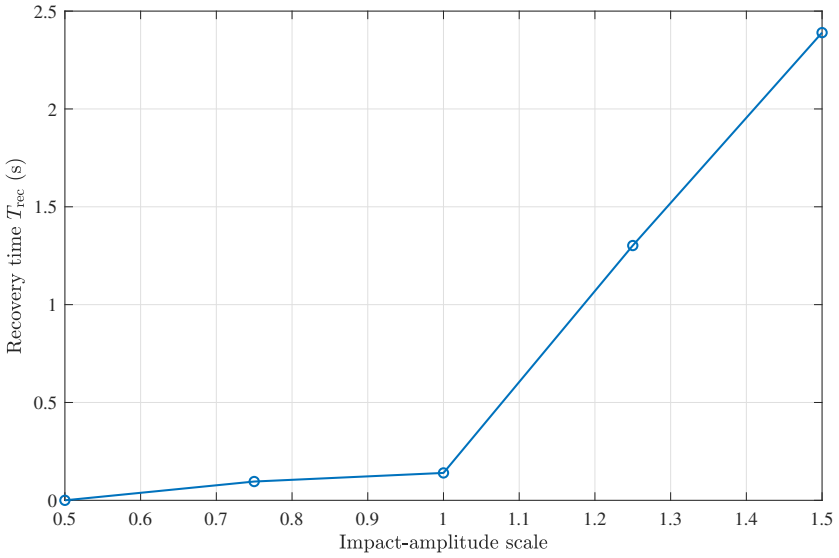


Figure 10. Recovery time versus impact-amplitude scale.

5.9. Randomized Robustness Evaluation

The deterministic trials above use a fixed perturbation realization. To quantify run-to-run sensitivity, a separate 24-trial paired study uses identical randomized configurations for the proposed and NFTSMC controllers. The payload mass is drawn uniformly from 18 to 50 kg; the impact amplitudes are multiplied by a factor in $[0.50, 1.40]$; the link-mass factors lie in $[0.92, 1.19]$ and $[0.92, 1.17]$; the gravity factor lies in $[0.96, 1.05]$; the friction factor lies in $[0.88, 1.24]$; and the position and velocity noise standard deviations are varied independently within the prescribed simulation ranges. All other controller settings, integration step, actuator limits, reference trajectories and original deterministic tests are unchanged. The random parameter matrix uses seed 20261008, and independent measurement-noise realizations use seeds 9001–9024. The mean, sample standard deviation, empirical 95th percentile of the combined RMSE, mean and standard deviation of IAE, and number of trial-wise symmetric-bound violations are reported in Table 9. Figure 11 shows the distribution of combined RMSE values across all paired runs. In these tests, the proposed controller reduced the mean combined RMSE from 0.0934 to 0.0396 rad, but at least one sampled violation of the symmetric error bound occurred in 16/24 proposed-controller trials, versus 22/24 baseline trials. Thus low average error does not imply forward invariance under all randomized saturation and impact configurations. The controller uses numerical clipping of the transformed coordinate if $|e_i|/\rho_i$ approaches unity; this safeguard preserves finite numerical operations but is not a barrier guaranteeing constraint invariance. The randomized-trial evaluation also records the maximum constraint overrun and actuator saturation percentage, distinguishing tracking accuracy from constraint-feasibility outcomes. Violation duration is retained in the trial-level data but is not included in the aggregate table. Table 10 summarizes the frequency, severity, and saturation characteristics of these violations. The paired sample and saturation statistics describe empirical robustness within the tested parameter ranges; they do not establish stochastic or global constraint stability.

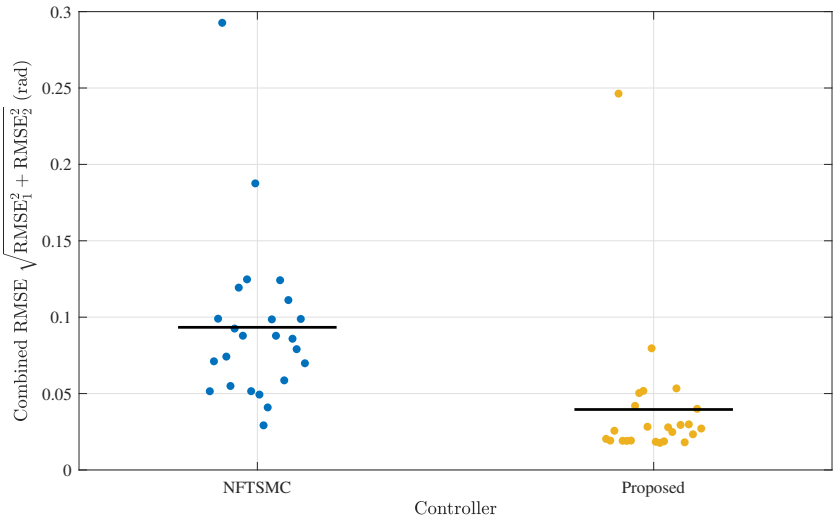


Figure 11. Distribution of combined joint RMSE for paired randomized disturbance and parameter trials. Horizontal bars mark sample means.

Table 9. Randomized robustness over 24 paired trials.

Controller	Mean RMSE	SD RMSE	P95 RMSE	Mean IAE	SD IAE	Viol. Runs
NFTSMC	0.0934	0.0545	0.1782	0.615	0.341	22/24
Proposed	0.0396	0.0466	0.0757	0.267	0.452	16/24

Table 10. Constraint-violation severity and actuator saturation in the 24 paired randomized trials. Overrun is defined as $\max_{i,k}(|e_i(t_k)| - \rho_i(t_k))_+$, in radians.

Controller	Violating Runs	Mean Overrun (rad)	Worst Overrun (rad)	Mean Sat. (%)	Sat. in Viol. Runs (%)
NFTSMC	22/24	0.1911	0.7634	6.92	7.46
Proposed	16/24	0.0372	0.3921	2.47	3.69

5.10. Finite-Memory Implementation and Computing Cost

The observer uses truncated Grünwald–Letnikov coefficients $c_j^{(\mu)} = (-1)^j \binom{\mu}{j}$ for the Caputo-type update with zero initialized observer state, while the integral reaching gain uses $c_j^{(\nu)} = \Gamma(j+\nu)/[\Gamma(\nu)\Gamma(j+1)]$. The history window is $L = 150$ samples with step $h = 0.002$ s, corresponding to a 0.300 s truncated memory horizon. For n joints, two history convolutions have $O(nL)$ work per control step. A real-time ring-buffer implementation requires $2n(L+1)$ historical state values plus $2(L+1)$ coefficients, or approximately 7.1 KiB for $n = 2$, $L = 150$ using double precision and excluding plant states, other buffers and application overhead. The present offline simulator retains complete trajectories for plotting and thus also uses $O(nN)$ logging storage. At $h = 0.002$ s, the requested update rate is 500 Hz; the theoretical operation count alone cannot establish deadline satisfaction.

Table 11 records the detected processor, RAM and mean MATLAB wall-clock timing for one 12 s numerical run on the machine executing the script. The processor, installed memory, and software environment are identified for the computer used to obtain these measurements. Mean wall-clock time per simulation step includes the numerical plant integration and logging overhead; it is not an estimate of isolated controller execution time. Hardware-in-the-loop or on-target worst-case execution-time tests remain necessary to make real-time guarantees.

Table 11. Hardware information, finite-memory settings, and offline MATLAB simulation timing. The reported mean includes numerical integration and data logging, not just isolated controller execution.

Processor	Intel(R) Core(TM) Ultra 5 225H
Installed RAM	31.43 GiB
MATLAB platform	PCWIN64
MATLAB version	24.2.0.2712019 (R2024b)
Sampling interval	0.002 s
Finite-memory window	150 samples (0.300 s)
Mean simulation wall time	0.460 s for one 12 s cycle
Mean wall time per numerical step	0.0766 ms

5.11. Saturation Margin and Constraint Feasibility

In the ideal continuous-time theorem, the sufficient condition is the uniform inequality $k_{r,i}^{\min} > W_i^*$ on an independently established forward-invariant operating region. A numerical time history, even when its instantaneous value satisfies $|w_i(t_k)| < K_{ri}(t_k) + K_{fi}m_{v,i}(t_k)$, cannot establish this uniform inequality for all times, all admissible initial states, or arbitrary disturbances. The actual implementation also employs measurement noise, command clipping, finite-memory operators, and numerical safeguarding of the transformed error. In particular, once $|e_i| \geq \rho_i$, the exact transformation is no longer defined, and its numerically clipped value must not be presented as a proof of symmetry-bound invariance. The randomized violations in Table 9 are consistent with this distinction, but their precise mechanism cannot be attributed to saturation alone without a joint examination of the applied torque, transformed residual, and constraint margin.

The deterministic combined-duty simulation records the applied saturation residual $\Delta\tau$, the sampled nominal matched-disturbance reconstruction, and the corresponding robust reaching gain for comparison. The residual is evaluated only on samples strictly

inside the symmetric bound; the comparison is diagnostic rather than a certified W_i^*. The sampled, jointwise results are reported in Table 12.

Table 12. Sampled matched-residual diagnostics for the deterministic extreme-duty case, restricted to the interior $|e_i(t_k)/\rho_i(t_k)| < 0.95$. These values are numerical diagnostics, not uniform continuous-time bounds on the saturated controller.

Joint	Peak Sampled $\lvert w_i \rvert$	Minimum Sampled $K_{r,i} + K_{f,i} m_{v,i}$	Positive-Margin Sample Fraction
1	90.26	16.90	0.922
2	1205.34	16.25	0.625

The positive-margin sample fractions are 92.2% for joint 1 and 62.5% for joint 2, so the sampled instantaneous comparison fails at 7.8% and 37.5% of the respective interior samples. Furthermore, the recorded peak $|w_i|$ exceeds the minimum sampled robust gain for both joints. These observations do not establish the uniform sufficient condition $k_{r,i}^{\min} > W_i^*$ in Theorem 2 for the simulated operating cycle, especially for joint 2. The fixed-time result must therefore be read as a conditional statement for the ideal continuous-time design; the tracking-error and constraint outcomes in the regularized saturated simulations are numerical observations, not applications of an independently verified fixed-time certificate.

6. Discussion

The proposed structure assigns distinct roles to the model compensation, disturbance reconstruction, symmetry constraint, and fixed-time dynamics. The nominal Euler–Lagrange model provides feedforward compensation, the momentum residual avoids numerical differentiation of velocity, the fractional observer reconstructs heavy-load uncertainty with memory, and the odd error transformation maps the zero-centered symmetric constraint into an unconstrained coordinate. The mixed-power reaching and terminal dynamics provide the fixed-time certificate, while the fractional integral modulates the robust reaching gain through a nonnegative memory state. This separation preserves the fixed-time argument without discarding the history-dependent information.

The deterministic and randomized tests reveal different levels of robustness. In the nominal extreme-duty example, the maximum constraint ratio remains below unity; in the broader randomized study, violations occur in a substantial fraction of trials, even though their mean tracking error is smaller than that of NFTSMC. The simulation results show complementary trends across tracking error, recovery time, and actuator demand. The CTC case has comparatively smooth torque but poor robustness, whereas conventional SMC and NFTSMC improve disturbance rejection with higher observed torque variation and more frequent saturation. The oscillations in the estimated load and applied torque during the heavy-payload interval reflect the specified measurement noise, momentum-filter bandwidth and the nonlinear feedback response; the numerical study does not establish a chattering-free implementation. Quantifying filtered-command total variation and actuator heating under hardware sampling remains necessary. The proposed controller achieves rapid post-impact recovery while maintaining the symmetric error bounds in the particular deterministic design extreme case, not in every randomized trial. The ablation study attributes the largest performance losses to removal of disturbance estimation and the symmetric-constraint transformation, while the fractional memory term provides an additional reduction in impact-recovery error and IAE.

Several limitations remain. First, the present study is numerical and uses a two-link heavy-duty benchmark rather than the full multi-DOF cutter-changing robot. Second, fractional operators require finite-memory or rational approximation on a real-time controller, so

computational burden and sampling-period sensitivity should be quantified experimentally. Third, the theoretical fixed-time result assumes that the transformed residual w remains below the available robust gain. Extremely severe saturation can violate this condition; the impact-amplitude sweep explicitly illustrates this physical limit. Fourth, the present lumped model treats uncertainty as matched in joint space. Flexible transmissions, severe backlash, structural modes, and contact constraints may introduce unmatched dynamics and should be addressed by an augmented flexible-joint or task-space force/impedance model.

For the intended shield-tunneling application, the next experimental stage should use identified link and tool parameters, actual gearbox or hydraulic-drive limits, cutter extraction-force records, encoder noise statistics, and the real task trajectory. The same evaluation protocol can then report RMSE, maximum error, IAE, torque energy, torque total variation, saturation ratio, observer error, and post-impact recovery time. Hardware-in-the-loop testing is also useful before full-scale deployment because it can quantify the computational cost of the finite-memory fractional operators and the sensitivity to communication delay.

7. Conclusions

This study investigated fixed-time anti-disturbance tracking of a heavy-duty cutter-changing manipulator with a zero-centered time-varying symmetric tracking-error set. The main methodological contribution is the coupling of an acceleration-free momentum residual and Caputo fractional-order observer with an odd error transformation and mixed-power terminal dynamics. A nonnegative fractional memory integral reinforces the reaching gain without becoming part of the sliding manifold. The filtered-input bound shows that finite-amplitude payload jumps do not invalidate the observer's Caputo regularity on a finite observation horizon. Theoretical statements comprise a componentwise Mittag–Leffler practical bound for observer error and conditional fixed-time bounds for the ideal sign-based controller when the explicit estimate-and-saturation residual budget is satisfied. The regularized, discrete implementation is not claimed to achieve exact fixed-time convergence under arbitrary saturation.

For the selected extreme-duty numerical test, the proposed controller achieved RMSE values of 0.0147 and 0.0135 rad, compared with 0.0157 and 0.0840 rad for NFTSMC. Its IAE decreased from 0.562 to 0.101 rad s (82.0%), while the first-impact recovery time fell from 0.358 to 0.096 s (73.2%). The largest sampled constraint ratio was 0.929, with actuator saturation present for 1.02% of the sampled cycle. These improvements are numerical observations for the stated plant and disturbances, not analytical performance guarantees for all payloads. In the randomized paired trials, the mean combined RMSE decreased from 0.0934 to 0.0396 rad, but 16 out of 24 runs of the proposed design showed one or more sampled constraint violations. These observations identify a clear limitation of the implemented regularized, saturated controller and motivate explicit anti-windup and constraint-aware actuator allocation.

Future work will address cutterhead-specific extraction-force measurements, identified multi-DOF mechanics, flexible transmissions, and experimentally measured noise. Hardware-in-the-loop and on-target 500-Hz tests should quantify execution-time variation and alternative short-memory or rational approximations of fractional operators. A constraint-aware torque-allocation or anti-windup auxiliary system is also needed to certify symmetric-bound invariance under severe saturation beyond the sufficient residual condition studied here.

Author Contributions: Conceptualization, S.Z. and G.Z.; methodology, S.Z., X.Z. and S.H.; software, S.Z.; formal analysis, S.Z., X.Z. and S.H.; investigation, S.Z., J.H., S.H. and X.Z.; data curation, S.Z. and J.H.; writing—original draft preparation, S.Z. and J.H.; writing—review and editing, S.H., X.Z.

and G.Z.; supervision, X.Z. and G.Z.; funding acquisition, G.Z. All authors have read and agreed to the published version of the manuscript.

Funding: This research was supported by the Research and Application of Key Technologies for Intelligent Equipment in Large-Diameter Shield Tunneling under Grant SBG20250000059.

Data Availability Statement: The data supporting the findings of this study are available from the corresponding author upon reasonable request.

Conflicts of Interest: Authors Shuaikun Zhang and Jialin Han were employed by the company China Railway Construction Heavy Industry Corporation Limited. The remaining authors declare that the research was conducted in the absence of any commercial or financial relationships that could be construed as a potential conflict of interest.

References

1. Spong, M.W.; Hutchinson, S.; Vidyasagar, M. *Robot Modeling and Control*; Wiley: Hoboken, NJ, USA, 2006.
2. Siciliano, B.; Khatib, O. (Eds.) *Springer Handbook of Robotics*, 2nd ed.; Springer: Cham, Switzerland, 2016.
3. Utkin, V.I. *Sliding Modes in Control and Optimization*; Springer: Berlin, Germany, 1992.
4. Bhat, S.P.; Bernstein, D.S. Finite-time stability of continuous autonomous systems. *SIAM J. Control Optim.* **2000**, *38*, 751–766. [CrossRef]
5. Polyakov, A. Nonlinear feedback design for fixed-time stabilization of linear control systems. *IEEE Trans. Autom. Control* **2012**, *57*, 2106–2110. [CrossRef]
6. Zhang, L.; Su, Y.; Wang, Z.; Wang, H. Fixed-time terminal sliding mode control for uncertain robot manipulators. *ISA Trans.* **2024**, *144*, 364–373. [CrossRef]
7. Arteaga, M.A. A nonsingular fixed-time sliding mode controller for robot manipulators in the presence of external perturbations and partially known model. *Int. J. Robust Nonlinear Control* **2025**, *35*, 2010–2026. [CrossRef]
8. Nguyen, V.T.; Bui, T.T.; Pham, H.Y.; Pham, N.T.; Nguyen, D.-K.; Mobayen, S. Reliable nonsingularity adaptive fixed-time sliding mode control under input saturation for an uncertain robotic manipulator. *Robot. Auton. Syst.* **2025**, *198*, 105326. [CrossRef]
9. Nguyen, D.-C.; Nguyen, T.-V.-A. Fixed-time active fault-tolerant control for cable-driven robots under tension constraints. *Eur. J. Control* **2026**, *89*, 101503. [CrossRef]
10. Bechlioulis, C.P.; Rovithakis, G.A. Robust adaptive control of feedback linearizable MIMO nonlinear systems with prescribed performance. *IEEE Trans. Autom. Control* **2008**, *53*, 2090–2099. [CrossRef]
11. Ghanooni, P.; Habibi, H.; Yazdani, A.; Wang, H.; MahmoudZadeh, S.; Ferrara, A. Prescribed performance control of a robotic manipulator with unknown control gain and assigned settling time. *ISA Trans.* **2024**, *145*, 330–354. [CrossRef]
12. Zhang, X.; Wang, R. Non-singular fast terminal sliding mode control of robotic manipulator with prescribed performance. *J. Eng. Appl. Sci.* **2024**, *71*, 217. [CrossRef]
13. Chen, X.; Su, B. Event-triggered optimal control based on prescribed performance for a two-link robotic manipulator. *Optim. Control Appl. Methods* **2025**, *46*, 114–134. [CrossRef]
14. Zhang, J.; Xia, M.; Wu, Z.; Li, S.; Liu, W. Predefined-time prescribed performance fault-tolerant control for robotic manipulator trajectory tracking. *Control Eng. Pract.* **2025**, *163*, 106397. [CrossRef]
15. Zhang, C.; Zhang, G.; Han, W.; Lv, X.; Shi, Z. Distributed fixed-time control for high-order multi-agent systems with FTESO and feasibility constraints. *J. Frankl. Inst.* **2024**, *361*, 107219. [CrossRef]
16. Shi, Z.; Han, W.; Zhang, C.; Zhang, G. A modular prescribed performance formation control scheme of a high-order multi-agent system with a finite-time extended state observer. *Electronics* **2025**, *14*, 1783. [CrossRef]
17. Shi, Z.; Zhang, C.; Zhang, G. Active disturbance rejection-based tracking control of robotic manipulators under a universal symmetry-constraint framework. *Symmetry* **2026**, *18*, 919. Correction in *Symmetry* **2026**, *18*, 1002. [CrossRef]
18. Chen, C.; Jia, L.; Chen, T.; Zhang, G.; Rong, X. Prescribed-performance optimal backstepping control for hydraulic manipulators with disturbance compensation. *ISA Trans.* **2026**, *177*, 692–708. [CrossRef]
19. Podlubny, I. *Fractional Differential Equations*; Academic Press: San Diego, CA, USA, 1999.
20. Diethelm, K. *The Analysis of Fractional Differential Equations*; Springer: Berlin, Germany, 2010.
21. Kilbas, A.A.; Srivastava, H.M.; Trujillo, J.J. *Theory and Applications of Fractional Differential Equations*; Elsevier: Amsterdam, The Netherlands, 2006.
22. Ahmed, S.; Azar, A.T.; Tounsi, M. Design of adaptive fractional-order fixed-time sliding mode control for robotic manipulators. *Entropy* **2022**, *24*, 1838. [CrossRef]
23. Dou, B.; Yue, X. Disturbance observer-based fractional-order sliding mode control for free-floating space manipulator with disturbance. *Aerosp. Sci. Technol.* **2023**, *132*, 108061. [CrossRef]

24. Chávez-Vázquez, S.; Lavín-Delgado, J.E.; Gómez-Aguilar, J.F.; Razo-Hernández, J.R.; Etemad, S.; Rezapour, S. Trajectory tracking of Stanford robot manipulator by fractional-order sliding mode control. *Appl. Math. Model.* **2023**, *120*, 436–462. [CrossRef]
25. Ahmed, S.; Azar, A.T. Fractional-order fixed-time non-singular sliding mode control for nonlinear robotic manipulators. *IFAC-PapersOnLine* **2023**, *56*, 8105–8110. [CrossRef]
26. Ahmed, S.; Azar, A.T. Adaptive fractional tracking control of robotic manipulator using fixed-time method. *Complex Intell. Syst.* **2024**, *10*, 369–382. [CrossRef]
27. Pan, J. Fractional-order sliding mode control of manipulator combined with disturbance and state observer. *Robot. Auton. Syst.* **2025**, *183*, 104840. [CrossRef]
28. Gaufan, K.B.; Aremu, M.B.; Alyazidi, N.M.; Nasir, A. Robust fractional-order sliding mode control for robotic manipulator system with time-varying disturbances. *Frankl. Open* **2025**, *12*, 100287. [CrossRef]
29. Zheng, H.; Zhang, C.; Xu, Y.; Yan, P.; Shi, Z.; Zhang, G. Fully Distributed Dynamic Event-Triggered Observer-Based H_∞ Consensus Control of Fractional-Order Multi-Agent Systems. *Fractal Fract.* **2026**, *10*, 624. [CrossRef]
30. Zhang, C.; Shen, H.; Ma, L.; Shi, Z.; Zhang, G. Dynamic event-triggered fixed-time practical distributed optimization and output consensus of incommensurate nonlinear fractional-order multi-agent systems with input saturation. *Fractal Fract.* **2026**, *10*, 591. [CrossRef]
31. Lu, C.; Zhang, C.; Xu, Y.; Yan, P.; Shi, Z.; Zhang, G. Resilient prescribed-time safe optimization for fractional-order multi-agent systems under false data injection attacks. *Fractal Fract.* **2026**, *10*, 521. [CrossRef]
32. Dou, B.; Yue, X. Fractional-order sliding mode control for free-floating space manipulator with disturbance and input saturation. *Int. J. Robust Nonlinear Control* **2025**, *35*, 3094–3115. [CrossRef]
33. Chen, W.-H.; Ballance, D.J.; Gawthrop, P.J.; O'Reilly, J. A nonlinear disturbance observer for robotic manipulators. *IEEE Trans. Ind. Electron.* **2000**, *47*, 932–938. [CrossRef]
34. Li, T.; Zhang, G.; Zhang, T.; Pan, J. Fixed-time sliding mode control for robotic manipulators based on disturbance observer. *Int. J. Aerosp. Eng.* **2024**, *2024*, 1263459. [CrossRef]
35. Li, T.; Zhang, G.; Zhang, T.; Pan, J. Adaptive neural network tracking control of robotic manipulators based on disturbance observer. *Processes* **2024**, *12*, 499. [CrossRef]
36. Yang, W.; Zhang, C.; Xu, Y.; Lu, C.; Yan, P.; Shi, Z. Fixed-time disturbance observer-based connectivity-preserving formation control for high-order multi-agent systems with actuator faults. *Actuators* **2026**, *15*, 418. [CrossRef]

Disclaimer/Publisher's Note: The statements, opinions and data contained in all publications are solely those of the individual author(s) and contributor(s) and not of MDPI and/or the editor(s). MDPI and/or the editor(s) disclaim responsibility for any injury to people or property resulting from any ideas, methods, instructions or products referred to in the content.